RESEARCH ARTICLE

ADVANCED
INTELLIGENT
SYSTEMS
Open Access

www.advintellsyst.com

Molecular Tailoring to Achieve Long-Term Plasticity in Organic Synaptic Transistors for Neuromorphic Computing

Naryung Kim, Gyeong-Tak Go, Hea-Lim Park, Yooseong Ahn, Jingwan Kim, Yeongjun Lee, Dae-Gyo Seo, Wanhee Lee, Yun-Hi Kim,* Hoichang Yang,* and Tae-Woo Lee*

Organic synaptic transistors (OSTs) using intrinsic polymer semiconductors are demonstrated to be suitable for neuromorphic bioelectronics. However, diketopyrrolopyrrole (DPP)-based copolymers are not applicable to neuromorphic computing systems because the DPP polymer film has demonstrated only short-term plasticity with short retention (<50 ms) in synaptic devices because of their intrinsic difficulty of electrochemical doping. To expand their applications toward neuromorphic computing that requires long-term plasticity, artificial synapses with extended retention time should be developed. Herein, molecular tailoring approach to extend the retention time in the ion-gel-gated OSTs that use DPP is suggested. The molecular structure is controlled by changing alkyl spacer lengths of side chains. As a result, the doping process is more favorable in DPP with long alkyl spacer, which is confirmed by high doping concentration and slow dedoping rate. Therefore, dedoping of ions is more suppressed in DPP with long alkyl side chain that exhibits extended retention time (≈800 s) of the OSTs. These optimized DPP-based OSTs obtain high pattern recognition accuracy of $\approx96.0\%$ in simulations of an artificial neural network. Molecular tailoring strategies provide a guideline to overcome the intrinsic problem of short synaptic retention time of the OSTs for use in neuromorphic computing.

1. Introduction

Biological nervous systems detect various stimuli,[1] perform learning and memorization activities,[2–4] and use the processed information to guide management of the bodies that they inhabit.[4,5] These processess entail transmission of a huge number of neural signals through a neural network that is composed of neurons connected by synapses.[1,4–6] During the processes, the synaptic plasticity of synapses contributes significantly to information flow, data processing, and memory functions.[4,7] Emulation of these biological synapses in artificial electronic synapses will have a wide range of applications including neural network, neuromorphic circuits, and optoelectronic neuromorphic system.[8–18]

Organic synaptic transistors (OSTs) have advantages of low energy consumption,[9,19,20] simple fabrication,[19,21] mechanical flexibility,[22] and biocompatibility.[23,24] Furthermore, the ion-gel-gated OSTs (IGOSTs) directly emulate the biological phenomena by which neurotransmitters diffuse through the synaptic cleft from the pre- to the postsynaptic membranes, that is, a presynaptic electrical

N. Kim, G.-T. Go, H.-L. Park, Y. Lee, D.-G. Seo, W. Lee, T.-W. Lee
Department of Materials Science and Engineering
Seoul National University (SNU)
1 Gwanak-ro, Gwanak-gu, Seoul 08826, Republic of Korea
E-mail: twlees@snu.ac.kr

H.-L. Park
Department of Materials Science and Engineering
Seoul National University of Science and Technology
232 Gongneung-ro, Nowon-gu, Seoul 01811, Republic of Korea

The ORCID identification number(s) for the author(s) of this article can be found under https://doi.org/10.1002/aisy.202300016.

Y. Ahn, H. Yang
Department of Chemical Engineering
Inha University
Incheon 22212, Republic of Korea
E-mail: hcyang@inha.ac.kr

J. Kim, Y.-H. Kim
Department of Chemistry
Gyeongsang National University and Research Institute of Green Energy Convergence Technology (RIGET)
Jinju 52828, Republic of Korea
E-mail: ykim@gnu.ac.kr

T.-W. Lee
School of Chemical and Biological Engineering
Institute of Engineering Research
Research Institute of Advanced Materials
Soft Foundry
Seoul National University
1 Gwanak-ro, Gwanak-gu, Seoul 08826, Republic of Korea

**ADVANCED
SCIENCE NEWS**

www.advancedsciencenews.com

**ADVANCED
INTELLIGENT
SYSTEMS**

www.advintellsyst.com

spike from a gate electrode drives migration of anions in an ion gel in p-type IGOSTs.[25,26] This ionic migration electrically generates a postsynaptic response in a drain electrode. OSTs are regarded as promising components of next-generation neuromorphic systems. However, the OSTs using intrinsic polymeric semiconductor films have often suffered from short synaptic retention time, which is not suitable for neuromorphic computing.[27]

Diketopyrrolopyrrole (DPP)-based donor–acceptor (D–A) derivatives (DPP–DAs) as semiconducting copolymers have been extensively investigated for organic transistors,[28,29] due to their advantages such as low cost,[30] mechanical flexibility,[31,32] high mobility, and tunable optoelectrical properties by molecular design.[33,34] However, DPP-DAs are not easily electrochemically doped by anion dopants[35] and thus have been employed only for neuromorphic bioelectronics to realize artificial nerves that mimic peripheral nerves of biological bodies because the film showed only short-term plasticity with short retention time (<50 ms).[9,22,36] Various OSTs with DPP-DAs cannot show long-term plasticity for neuromorphic computing, and their use is still limited to artificial peripheral nervous systems, which require only short decay time in synaptic devices. To expand their applications toward neuromorphic computing that requires long retention time, artificial synapses with extended retention times should be developed.[37–39] The decay behavior of DPP-based OSTs (DPP-OSTs) depends on charge dynamics of ion migration, trapping, and detrapping occurring around the interfaces between organic semiconducting (OSC) layer and ion gel under a pulsed gate bias.[19,26] This is affected by the interaction between OSC films and ions in the ion gels.[25] Thus, the molecular interaction and resultant microstructure of DPP-DAs must be engineered to yield the desired properties, but this task requires understanding of the relationship between the structural characteristics and the synaptic characteristics of DPP-OSTs.

Here, we demonstrated a facile approach that uses molecular engineering to control synaptic retention time of the DPP-OSTs. To investigate how the molecular structures of DPP-DAs affect synaptic decay behavior of the DPP-OSTs, we changed the lengths of the alkyl spacers of the side chains in the DPP-DAs and then found that the molecular engineering also controls the microstructures of the DPP-DA films. It was found that the synthesized DPP-based copolymer with longer alkyl spacer-branched side chains showed excellent π-conjugated ordering in both nonannealed and annealed films, where the polymer chains were oriented in an edge-on form with respect to the film surface, in comparison to the short alkyl spacer DPP-based copolymer where closely attached side-chains hindered the planarity of π-conjugated backbones. The resulting DPP-DA films could produce distinct decay characteristics in DPP-OSTs; a combination of extended linear alkyl spacer and appropriate thermal treatment improved π-conjugated ordering of the DPP-DAs with increasing grain sizes and extended the retention time of the DPP-OSTs. Especially, the time-dependent doping levels of the DPP-based copolymer films with different side-chain lengths were systematically characterized using UV–visible absorption analysis to isolate bulk doping effect from the three-terminal device structures. The results strongly supported that, DPP-DA with long alkyl side chain allows high doping concentration and slow dedoping rate. Finally, use of the optimal condition of DPP-OSTs (longer side chain with

thermal treatment) for neuromorphic computing achieved simulated ≈96.0% recognition accuracy of MNIST handwritten digits.

2. Results and Discussion

DPP-OSTs were fabricated with a top-gate, top-contact structure. Dilute solutions of diketopyrrolopyrrole selenophene-vinylene-selenophene (DPP-SVS) copolymers in chlorobenzene were spin cast to form OSC layers on glass substrates that were treated using self-assembled monolayers (SAMs), and ion gels were used as gate insulators (**Figure 1**a). In the devices, a metal probe tip of a gate electrode mimics the axon of the preneuron and fires a presynaptic electrical spike to drive anions to diffuse through the ion gel toward OSC layers. The drain electrode is considered to be the dendrite of the postneuron.

For molecular engineering, we synthesized two types of DPP-SVS polymers, one ("24SVS") has short alkyl spacer groups of C1 (total 24 carbons in the alkyl side chain) (Figure 1b) and the other ("29SVS") has long alkyl spacer groups of C6 (total 29 carbons in the alkyl side chain) between the branched alkyl side chains and DPP moieties (Figure 1c).[33,40] To investigate effects of microstructures in DPP copolymers, some samples were thermally annealed at 200 °C for 10 min after spin coating of each solution, that is, four types of DPP-SVS films were prepared: films that had been dried at room temperature without thermal annealing (24SVS_RT; 29SVS_RT) and films that had been annealed (24SVS_Ann; 29SVS_Ann). The films (both 24SVS and 29SVS) have ≈30 nm of thickness which was confirmed by atomic force microscopy (AFM). From previous research that measures thermogravimetric analysis (TGA) and differential scanning calorimetry (DSC) curve of 24SVS and 29SVS, the thermal annealing at 200 °C only induces crystallinity change and does not induce thermal degradation.[40,41]

In UV–vis absorption spectra of the four types of DPP-SVS copolymer films, all the spectra showed dual-band absorption peaks broadly ranging from 400 to 1000 nm, originating from the intramolecular charge transfer in D–A copolymers (Figure 1d,e).[33,42] 29SVS films had a maximum vibrational peak of around 800 nm, which was red shifted by ≈20 nm compared to the peak of 24SVS films. The shift mainly occurs because of the existence of the long alkyl spacer of C6 in the side chains, which could drastically decrease a steric hindrance of the bulky branched end group ($C_{22}H_{36}$) of the side chain to form planar π-conjugated structures, resulting in a more close-packed planar structure even in the as-spun film.[34,40,42] In 24SVS films, closely attached alkyl branches hindered the planarity of π-conjugated backbones. After annealing, the UV–vis absorption peaks of both the 24SVS and 29SVS films were slightly redshifted, which indicated an enhanced π–π stacking by facilitating the molecular reorganization. For 29SVS, which can form intrinsically better π-conjugated backbones even under a fast solvent evaporation condition, however, the short-time annealing did not much change the UV–vis absorption spectrum. These results are consistent with previous studies.[40]

For more quantified structural analysis, chain ordering and orientation in these cast films were revealed using 2D grazing-incidence X-ray diffraction (2D GIXD). The 2D GIXD patterns showed clear reflections at ($h00$) and (020), oriented along the Q_z and Q_r axes, respectively (**Figure 2**). The presence of

ADVANCED
SCIENCE NEWS
www.advancedsciencenews.com

ADVANCED
INTELLIGENT
SYSTEMS
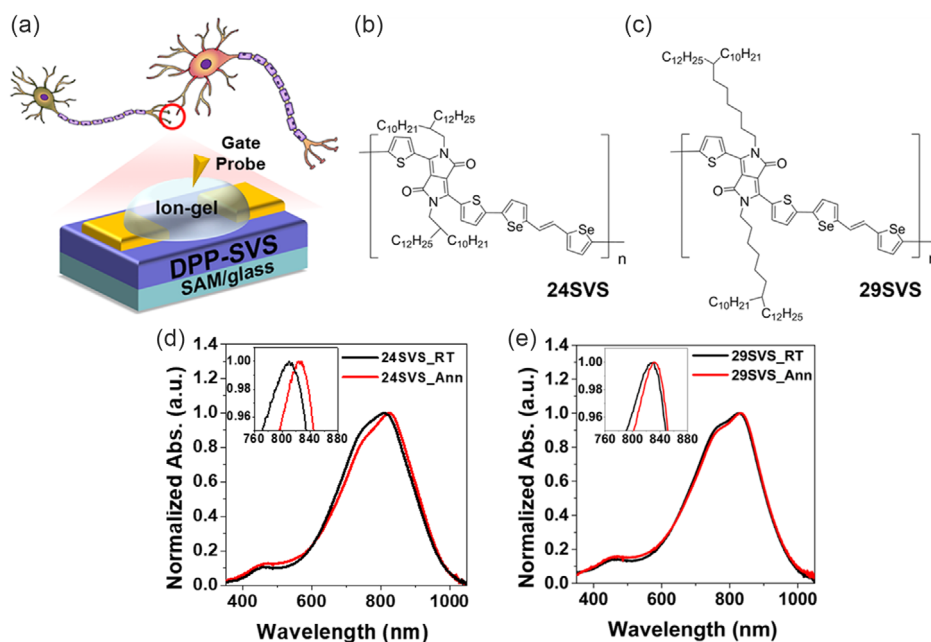Open Access

www.advintellsyst.com

Figure 1. Schematics of a) device structure of the DPP-OSTs with DPP-SVS polymers and chemical structure of b) 24SVS and c) 29SVS. Normalized UV–vis absorption spectra of d) 24SVS and e) 29SVS before (RT) and after thermal treatment at 200 °C for 10 min (Ann).

highly ordered X-ray reflections related to (h00) crystal planes suggests that all the DPP-SVS derivatives were favored to be oriented with an edge-on chain conformation on the substrates. Under the same thermal annealing condition, the 29SVS films displayed more distinct X-ray reflections with narrower full width at half maximum (FWHM) than the 24SVS films; the 29SVS films had ordered chain packing with preferential edge-on orientation on the substrate. After thermal annealing, both (h00) and (020) peaks became distinct; this evolution implies that the chain ordering of the DPP-SVS polymers was increased, and π-conjugated plane orientation amplified. As a result, 1D out-of-plane (Q_z) and in-plane (Q_r) X-ray diffraction profiles (Figure 2b,c) showed that the ordering and orientation of the π-conjugated planes decreased in the order: 29SVS_Ann > 29SVS_RT > 24SVS_Ann > 24SVS_RT. The lattice parameters of the four-type DPP-SVS films were extracted from the 2D GIXD patterns and are summarized in **Table 1**. The FWHM at (200) reflection was the lowest value of 0.053 in 29SVS_Ann and the highest one of 0.104 in the 24SVS_RT film. The average grain size (G, referred as coherence length) of these DPP-SVS derivative films was calculated using the following Scherrer Equation $G = k\lambda/\beta\cos\theta$, where k is 0.9, λ is the wavelength of the X-ray, and β is the FWHM of the (200) reflection.[43] These observations indicated that G was the largest value of 21.4 nm in 29SVS_Ann films and the smallest of 10.9 nm in 24SVS_RT films. The trend of G was 29SVS_Ann > 29SVS_RT > 24SVS_Ann > 24SVS_RT. In addition, π–π stacking distance, $d_{(020)}$ spacing became shorter in the 29SVS films of 3.65 Å than 3.80 Å (for the 24SVS system). The difference occurs because, as previously demonstrated in UV–vis absorption spectra, the long alkyl spacer in 29SVS minimizes the steric hindrance of the alkyl side branches, resulting in more excellent π-conjugated ordering.[40] AFM morphologies

(Figure S1, Supporting Information) of these films showed percolated nanodomains. In addition, root-mean-squared roughness values were between 0.85 and 1.05 nm, that is, the overall DPP-SVS film morphologies were not significantly affected by either the alkyl chain length or the thermal treatment.[33,44] However, π-conjugated chain packing and orientation could be finely modulated by alkyl spacer length and thermal treatment.

For typical IGOSTs including these DPP-SVS films, current–voltage (I–V) transfer curves (Figure S2, Supporting Information) showed large clockwise hysteresis during gate voltage sweeping.[25,26] This trend is attributed to ion doping and dedoping of the π-conjugated polymer layers in the operating IGOSTs. At the same thermal annealing condition (RT or Ann), 29SVS films produced higher drain current (I_D) than 24SVS one in DPP-OSTs, because the long separation of the alkyl branches from the conjugated backbone in 29SVS was known to drive better charge transport paths along π-conjugated planes formed by the DPP-based derivatives.[34,40] Additionally, short-time annealing at 200 °C increased I_D, originating from the extension of π-conjugated structure, as demonstrated by the UV–vis absorption spectra and GIXD results.

DPP-OSTs that used the four types of the DPP-SVS had different synaptic properties. Recent research on microstructural change of electrolyte/OSC interfaces has revealed that the ions are initially trapped in the amorphous region, but the depth of ion penetration into the OSC layer can be expanded to the side chains of the crystalline regions by increasing the amplitude, number, and frequency of stimulations.[45–47] The trapped ions, especially those trapped in crystallites, cannot easily diffuse back to the ion gel, so an excitatory postsynaptic current (EPSC) decays slowly.[25]

All devices showed spike-number dependent plasticity (SNDP) (**Figure 3**a). EPSCs were triggered by applying various numbers of spikes. In all the DPP-OSTs, the EPSC induced by a single
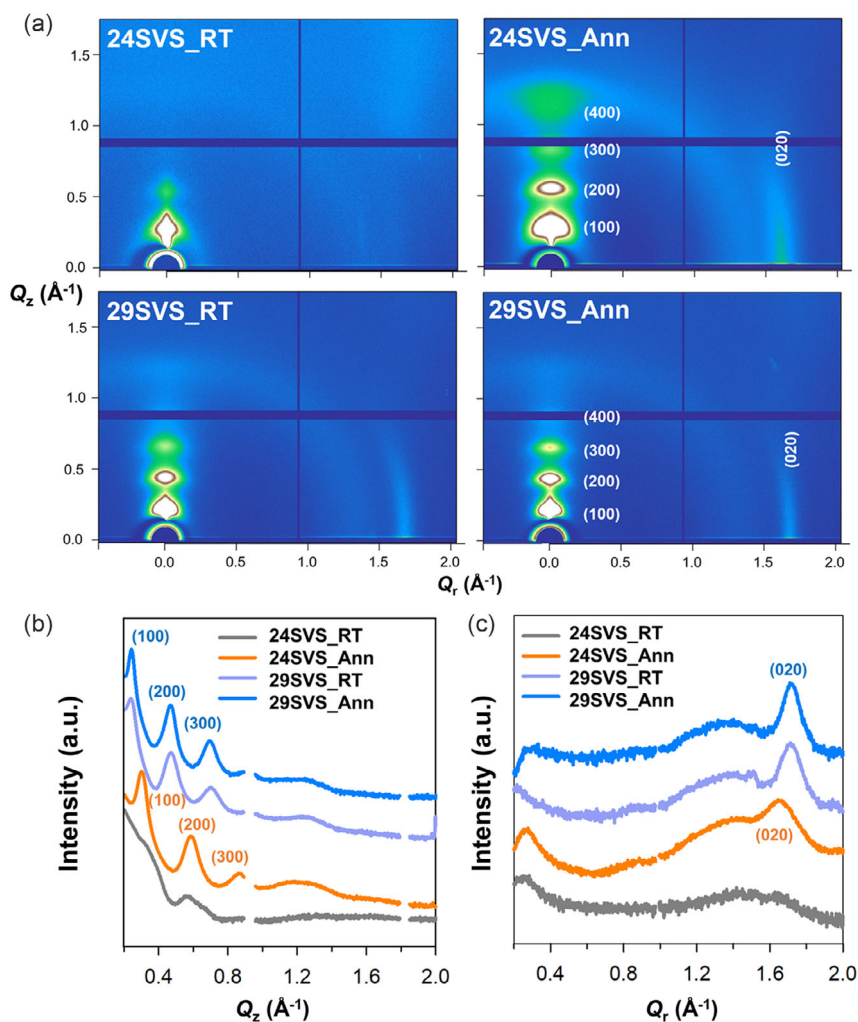
Figure 2. a) 2D GIXD patterns and b) 1D out-of-plane (Q_z) and c) in-plane (Q_r) X-ray profiles of four-type DPP-SVS films.

Table 1. Lattice parameters of four-type DPP-SVS copolymer films extracted from 2D GIXD patterns.

Film Type	(100) peak Lamella distance [Å]	(020) peak π–π stacking distance [Å]	FWHM$_{(200)}$ [Å^{-1}]	$G(= k\lambda/\beta\cos\theta)$ [nm]
24SVS_RT	22.42	3.80	0.104	10.9
24SVS_Ann	20.84	3.80	0.072	15.8
29SVS_RT	26.23	3.65	0.067	16.9
29SVS_Ann	25.83	3.65	0.053	21.4

spike decayed quickly, but as the number of spikes was increased, the EPSC increased, and the decay time increased:[48] this trend emulates biological synaptic plasticity which occurs when successive action potentials arrive at a preneuron and increase the quantity of neurotransmitters that are released into the synaptic cleft, thereby amplifying the ionic signal and strengthening the postsynaptic potential; this is an effective way to regulate the importance of chemical information in biological systems.[3,4,7] When one spike was applied, EPSCs were lower in the annealed films (24SVS_Ann and 29SVS_Ann) than in the nonannealed films (24SVS_RT and 29SVS_RT). However, after several spikes, EPSCs were higher in the annealed films (24SVS_Ann and 29SVS_Ann) than in the nonannealed films (24SVS_RT and 29SVS_RT); this change is mainly attributed to the fact that the annealed films (24SVS_Ann and 29SVS_Ann) had higher chain ordering and larger grain size than the nonannealed films (24SVS_RT and 29SVS_RT). 24SVS_Ann and 29SVS_Ann have well-ordered π-conjugated structures, large grain size, and small grain boundary density, so that bis(trifluoromethylsulfonyl)imide ([TFSI]$^-$) anions from the ion gel cannot easily penetrate the annealed films. Therefore, when stimulated with only one spike, these films had lower EPSC levels than the nonannealed films. However, several spikes are sufficient to drive [TFSI]$^-$ anions into both the amorphous and crystalline regions;[45,46] these trapped [TFSI]$^-$ anions could not easily escape from the bulk film, so successive spikes amplified the EPSC, and its decay time increased.
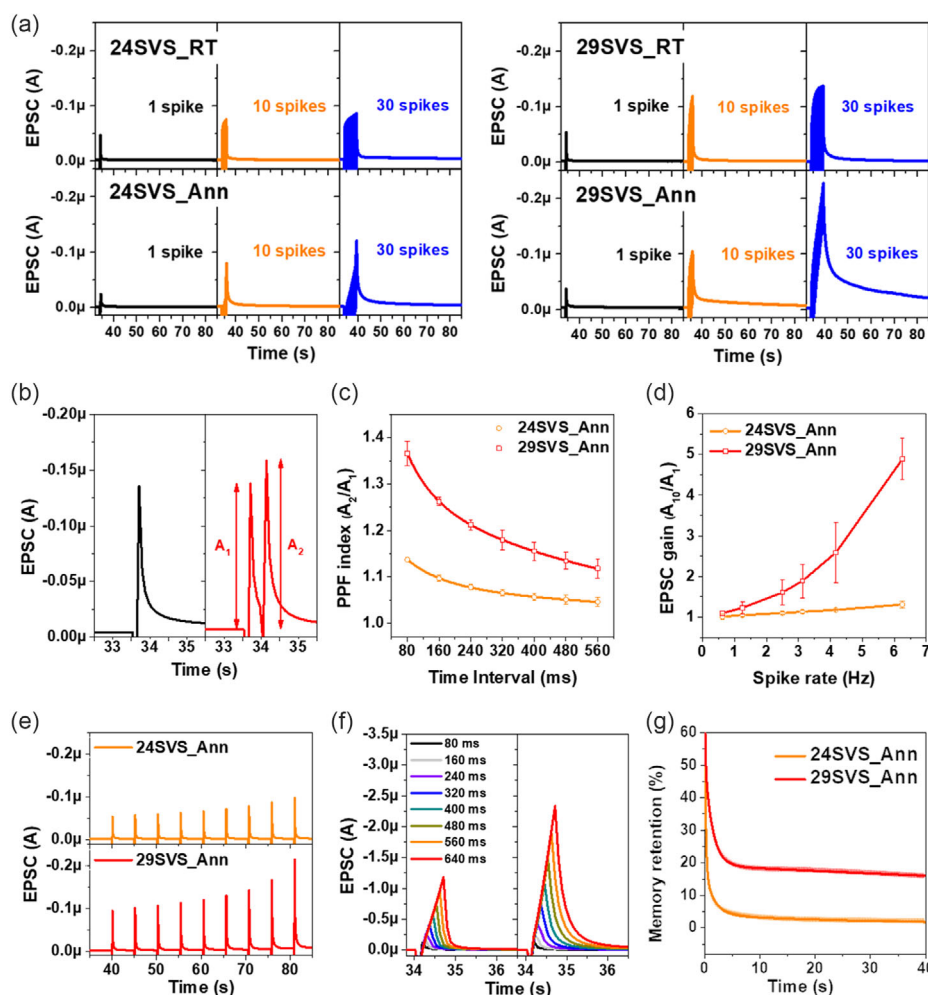
Figure 3. Spike number-dependent plasticity of the DPP-OSTs using a) 24SVS_RT, 29SVS_RT, 24SVS_Ann, and 29SVS_Ann films with 1, 10, and 30 spikes (spike voltage = −2 V, spike duration = 80 ms, spike interval = 80 ms). Synaptic characteristics of the DPP-OSTs with 24SVS_Ann and 29SVS_Ann. b) EPSC triggered by a single spike (left) and by two consecutive spikes (right). c) PPF index as a function of time interval from 80 to 560 ms. d) EPSC gain of A_{10}/A_1 with different spike frequencies from 0.625 to 6.25 Hz. e) Spike voltage-dependent plasticity from −2.5 to −3.3 V. f) Spike duration-dependent plasticity of 24SVS_Ann (left) and 29SVS_Ann (right) from 80 to 640 ms. g) Synaptic decay time by fitting the SNDP curves after 50 spikes with triexponential functions (spike voltage = −3 V, spike duration = 80 ms, spike interval = 80 ms).

The side chain-dependent chain ordering and orientation of DPP-SVS affected the EPSC response. The 29SVS samples (high chain ordering and orientation, large grain size) achieved higher EPSC than the 24SVS samples under 1, 10, and 30 spikes (Figure 3a). One different trend to note is that the annealed films (24SVS_Ann and 29SVS_Ann) showed the lower EPSC under 1 spike than nonannealed films (24SVS_RT and 29SVS_RT) despite their higher chain ordering in films. $\pi - \pi$ stacking distances were narrower in 29SVS than in 24SVS, in addition to the more ordered π-conjugated structures and larger grain size in 29SVS than in 24SVS. As for side chain length, the effect of this compact $\pi - \pi$ stacking distance is combined with the high π-conjugated ordering and large domain size. Accordingly, DPP-OSTs that used 29SVS had high EPSC while applying multiple gate voltage spikes. When 30 spikes were applied, the EPSC after 40 s from the stimulation was 873% relative to the initial baseline for 29SVS_Ann case, whereas it was 217% for 24SVS_Ann.

This difference can be caused from both doping concentration and charge mobility difference due to higher ordering and larger grain size of the 29SVS copolymers than the 24SVS films, which indicates that this side-chain engineering increased long-term potentiation (LTP), which is crucial to implement long-term memory behavior for neuromorphic computing.[49,50] All results indicate that the doping concentration of the DPP channel by ions is a key parameter to modulate the synaptic properties, especially short-term potentiation (STP) and LTP, in the DPP-OSTs. The 29SVS_Ann device with the highest ordering and largest domain size showed the highest EPSC and longest decay time (Figure 3a). The DPP-OSTs showed paired-pulse facilitation (PPF), which is a representative characteristic of STP.[51] (Figure S3, Supporting Information). To measure the PPF characteristics, two consecutive spikes were applied, separated by a time interval Δt. If the second spike was applied before the current induced by the first spike decayed to the initial value, the

ADVANCED
SCIENCE NEWS
www.advancedsciencenews.com

ADVANCED
INTELLIGENT
SYSTEMS
Open Access

www.advintellsyst.com

EPSC induced by the second spike is higher than the first one.[51,52] This temporal synaptic plasticity is expressed as PPF index of A_2/A_1, where A_1 is the first of the EPSC and A_2 is the second peak. In all the devices, PPF index increased as $80 \leq \Delta t \leq 560$ ms decreased. 29SVS_Ann had the highest PPF index ≈ 1.37 at $\Delta t = 80$ ms. In contrast, the 24SVS_RT showed the lowest PPF index ≈ 1.13 at $\Delta t = 80$ ms.

The typical EPSC of the IGOSTs (Figure 3b) showed an increased response to the second stimulus after the first stimulus. DPP-OSTs that used 24SVS_Ann showed different PPF than DPP-OSTs that used 29SVS_Ann (Figure 3c). Two consecutive electrical spikes ($80 \leq \Delta t \leq 560$ ms) were applied to the gate electrode of each DPP-OST. In both devices, as Δt decreased, PPF index increased. PPF index can be empirically approximated using a double-exponential decay term as

$$PPF = 1 + C_1 \exp(-\Delta t/\tau_{c1}) + C_2 \exp(-\Delta t/\tau_{c2}) \quad (1)$$

where C_1 and C_2 represent phase-facilitation magnitudes,[52] τ_{c1} is the characteristic relaxation time (tens of milliseconds) of the rapid phase, and τ_{c2} is the characteristic relaxation time (hundreds of milliseconds) of the slow phase. Curve-fitting yielded $\tau_{c1} = 66.48$ ms and $\tau_{c2} = 583.3$ ms for the 24SVS_Ann device and $\tau_{c1} = 91.65$ ms and $\tau_{c2} = 811.0$ ms for the 29SVS_Ann device. The increased length of the chain length extended the time constants.

The fabricated DPP-OSTs also showed spike-rate-dependent plasticity (SRDP).[49] (Figure 3d). Ten consecutive spikes were applied, and the SRDP property was quantified by EPSC gain of A_{10}/A_1, where A_{10} is the peak value of EPSC after the tenth spike, and A_1 is the peak value after the first spike. The EPSC gain of A_{10}/A_1 was measured with various rates of electrical pulse trains. As spike rate increased from 0.625 to 6.25 Hz, the EPSC gain of A_{10}/A_1 increased; this change emulates high-pass filtering characteristics of the biological synapse.[49,50,53] The 29SVS_Ann with slow decay time had higher A_{10}/A_1 ($\approx 500\%$ at 6.25 Hz) than did 24SVS_Ann ($\approx 130\%$ at 6.25 Hz). At 6.25 Hz, the EPSC after 40 s from electrical pulse stimulation was 405% relative to the initial baseline for 29SVS_Ann case, whereas it was 183% for 24SVS_Ann, demonstrating longer retention property of the 29SVS_Ann device (Figure S4, Supporting Information).

The strength of EPSC was effectively modulated by the spike amplitude and the width of voltage spikes (Figure 3e,f). As the spike number and amplitude were increased, the EPSC increased, because increased synaptic input by high voltage and extended pulse duration increased the number of [TFSI]$^-$ anions that penetrated the bulk DPP-SVS films. These synaptic characteristics with various voltage amplitude and spike duration showed similar trends to other synaptic characteristics, that is, higher EPSC and slower decay properties in 29SVS_Ann devices than in 24SVS_Ann ones.

To compare the LTP properties, the decay time was obtained by the EPSC decay curves after 50 spikes to triexponential functions (Figure 3g).

$$I = I_0 + I_1 \exp(-t/\tau_1) + I_2 \exp(-t/\tau_2) + I_3 \exp(-t/\tau_3) \quad (2)$$

where I_0 is the initial current, I_1, I_2, and I_3 are prefactors of EPSC, and τ_1, τ_2, and τ_3 are their characteristic relaxation time. τ_1 is the relaxation time constant which corresponds to the

backdiffusion of ions from electrical double layer, and time constants of τ_2 and τ_3 are related to dedoping of [TFSI]$^-$ anions from amorphous and crystalline regions, respectively.[25] Time constants of τ_1, τ_2, and τ_3 of 24SVS_Ann are 0.36, 2.79, and 45.78 s, respectively, and these values are respectively increased to 0.31, 1.58, and 151.51 s, for 29SVS_Ann device. The 29SVS_Ann device showed higher τ_3 value of decay time, which is related to LTP, than the 24SVS_Ann device, so 29SVS_Ann showed longer retention than the 24SVS_Ann case. These results suggested that the synaptic weight retention can be tailored by proper microstructural modulation and side-chain engineering, and this approach is feasible toward neuromorphic computing. Compared with previously published DPP-OSTs, 29SVS_Ann device shows longer retention time (Table S1, Supporting Information).

Low energy consumption is also one of important advantages of neuromorphic computing. The energy consumptions of IGOSTs are estimated as $E \approx V_D * I_D * t$, where $V_D = 50$ mV is drain voltage, $I_D = 19.2$ nA (24SVS_Ann), 19.3 nA (29SVS_Ann) is drain current, and $t = 20$ ms is spike duration, respectively (Figure S6, Supporting Information). The estimated energy consumptions $E \approx 19.2$ (24SVS_Ann), and 19.3 pJ (29SVS_Ann) is comparable to other IGOSTs that enable energy-efficient computing systems (Table S2, Supporting Information).

To isolate the effect of bulk doping in the 24SVS_Ann and 29SVS_Ann films, we conducted time-dependent UV–vis absorption spectral measurements during real-time electrochemical reaction of two different DPP-SVS films (24SVS_Ann and 29SVS_Ann) in the ion-gel (**Figure 4**). This approach excluded the complex carrier dynamics that occur in three-terminal device structures. During a 30 s doping process, a voltage was continuously applied to DPP polymer films that were coated on ITO glasses. The bluish color of DPP-SVS films clearly became transparent (Figure 4b, dashed line); this is evidence of electrochemical reaction.[54] Then a 45 s dedoping process was conducted without any electrical bias to confirm reverse electrochemical reaction ; after this process, the film color returned to its the initial bluish (Figure 4b, red box). To quantify the doping and dedoping levels in the two films, the absorption spectra were normalized to facilitate comparison (Figure 4c,d). The normalized absorption decreased during the doping process; specifically, the dual-band peaks of the DPP-SVS films gradually disappeared. This change implies that the both amorphous and crystalline regions become oxidized.[46] During the dedoping process, the absorbance curves of both 24SVS_Ann and 29SVS_Ann films returned to the initial states.[46]

This electrochemical reaction can be simplified by presenting only the changes of the maximum absorption peaks (Figure 4e). At 30 s, the normalized maximum absorption peak of the 29SVS_Ann spectrum was reduced to <0.6, whereas that of the 24SVS_Ann film decreased only to 0.9. This result confirms that the effective doping level was higher in 29SVS_Ann film than in 24SVS_Ann film. The effective doping rate is determined by the net balance between doping and dedoping dynamic behaviors. The trapped anions in the large-grain and highly ordered π-conjugated bulk film of 29SVS_Ann could not easily diffuse back to the ion gel.[45–47] Thus, the effective doping rate was higher in the 29SVS_Ann film than in the 24SVS_Ann, so the absorbance of the 29SVS_Ann film decreased sharply during
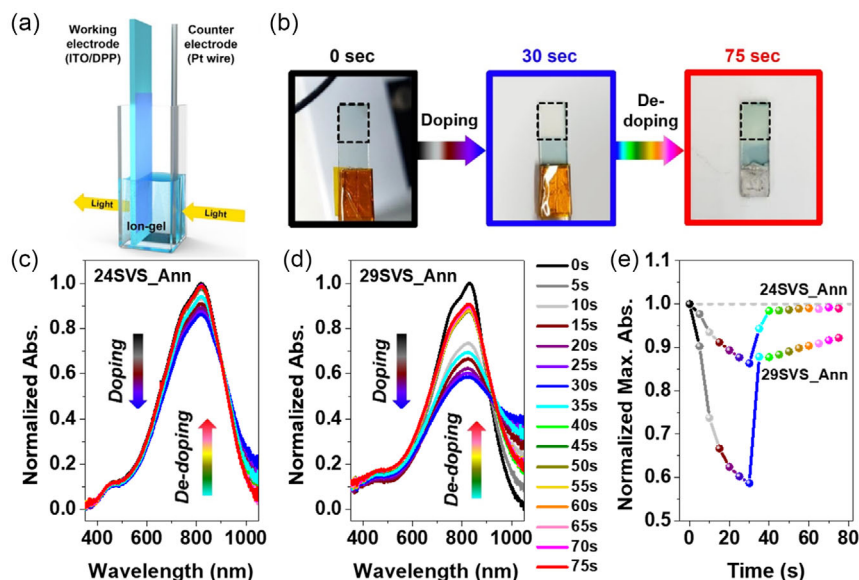
**ADVANCED
SCIENCE NEWS**

www.advancedsciencenews.com

**ADVANCED
INTELLIGENT
SYSTEMS**
Open Access

www.advintellsyst.com

Figure 4. a) Schematic of experimental setup to measure time-dependent UV–vis spectra during real-time electrochemical reaction of the DPP-SVS films in the ion gel during electrochemical reaction. b) Optical images of the 29SVS_Ann film at initial state (black box), after doping for 30 s (blue box) and after dedoping for 45 s (red box). Normalized time-dependent absorption spectra of c) 24SVS_Ann and d) 29SVS_Ann films. From 0 to 30 s, doping was performed, and from 30 to 75 s, dedoping was processed. e) Time evolution of normalized values of maximum absorption peaks from (c,d).

the doping process. After 30 s, a dedoping process was executed, so the reduced absorbance spectra recovered toward the initial state; this change is evidence of dedoping behavior. The 24SVS_Ann film completely returned to its initial state after dedoping, but the 29SVS_Ann film maintained some of its doping level (≈0.9). This phenomenon is consistent with the slowed synaptic decay of the 29SVS_Ann device, in that slowing requires extension of the duration for which anions remain in the film.

The ionic transport is generally faster in the amorphous region than the crystalline region.[55,56] Because 24SVS_Ann film exhibits lower crystallinity than 29SVS_Ann film, 24SVS_Ann film is expected to have faster ionic transport than 29SVS_Ann film. Therefore, 24SVS_Ann film was expected to have a higher doping rate and faster dedoping rate than 29SVS_Ann film. However, 29SVS_Ann film shows a higher doping rate and slower dedoping rate

than 24SVS_Ann. Therefore, doping of [TFSI]⁻ anions in 29SVS_Ann is considered electrochemically more favorable than doping in 24SVS_Ann. We suggested that this electrochemical preference of doping process is due to steric hindrance between branched alkyl side chains and doped ions (**Figure 5**). The DPP with a long alkyl side chain (both 24SVS_Ann and 29SVS_Ann) has steric hindrance between side chains.[41,57] The 29SVS_Ann film is less sterically hindered than 24SVS_Ann, which is proved by the redshift of UV–vis absorption spectra. The introduction of ions that induces lattice expansion of lamellar spacing will be more hindered in the 24SVS_Ann film than in the 29SVS_Ann films: doping in 29SVS_Ann will be more facilitated by the low steric hindrance (Figure 5, left) while doping in 24SVS_Ann will be more difficult by high steric hindrance (Figure 5, right).
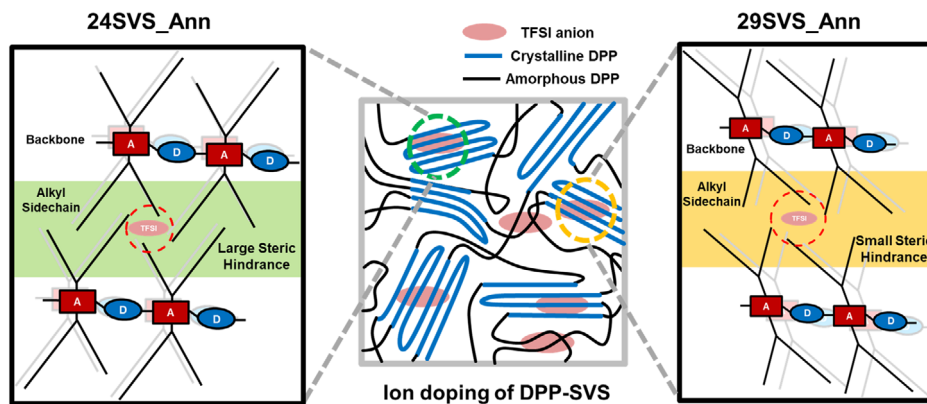

Figure 5. Schematic diagram of hypothesized mechanism. 24SVS_Ann film exhibits large steric hindrance between alkyl side chain and doped [TFSI]⁻ anions (left), and 29SVS_Ann film exhibits small steric hindrance (right).

ADVANCED
SCIENCE NEWS

www.advancedsciencenews.com

ADVANCED
INTELLIGENT
SYSTEMS
Open Access

www.advintellsyst.com

Because of the difference in the doping/dedoping process between 24SVS and 29SVS, STP and LTP behaviors can be explained. 29SVS_Ann device shows a higher PPF ratio and EPSC gain in SRDP than 24SVS_Ann device. For STP, larger amounts of [TFSI]$^-$ anions will be doped into the amorphous region of 29SVS_Ann film than 24SVS_Ann film, resulting in a higher PPF ratio and EPSC gain in SRDP. For LTP, crystallinity of DPP and steric hindrance will both affect the decaying property. This is well matched with EPSC of 29SVS device that is larger than that of the 24SVS device. 29SVS_Ann exhibits the largest EPSC because of high doping rate of 29SVS and improved charge transport after thermal annealing. The large domain and highly ordered π-conjugated 29SVS_Ann film had a longer synaptic retention time than 24SVS_Ann film.[18,19] Also, doping of [TFSI]$^-$ anions is electrochemically preferred in 29SVS_Ann device, so large amounts of anions are doped in the 29SVS_Ann films and dedoping shows slow decay in 29SVS_Ann IGOST. IGOST with 29SVS shows a larger increase in retention time after thermal annealing than IGOST with 24SVS. The steric hindrance effect becomes more strengthened in highly crystalline samples because the crystalline regions are more closely ordered than the amorphous region; therefore, steric hindrance mainly affects the electrochemical doping into the crystallite. For highly crystalline (thermally annealed) samples, the retention time was significantly increased by molecular engineering. To enhance the effect of molecular engineering, microstructural engineering is required to achieve long retention times for neuromorphic computing applications. These results demonstrate the utility of side-chain engineering and thermal treatment for modulation of chain ordering and domain size to tailor the synaptic decay characteristics of the DPP-OSTs. We concluded that the IGOST with the 29SVS_Ann is an optimal condition to achieve long synaptic retention.

To demonstrate the viability of the optimized IGOST as neuromorphic computing components, we considered an artificial neural network (ANN) composed of a crossbar array of the optimized IGOST (29SVS_Ann). The pattern recognition using ANN was simulated using the MNIST database of handwritten digits (**Figure 6**).[58,59] The ANN consists of 8×8 and 28×28 pixels, which are computed as 64 and 784 input neurons (preneurons). 300 neurons were used as a hidden layer for the backpropagation algorithm and 10 output neurons (postneurons) were used to represent digits from 0 to 9. To make the discrete conductance states, 50 negative pulse trains of −3.0 V and 50 positive pulse trains of +1.2 V were used with constant drain voltage of −0.4 V. Because the conductance state has a volatility which limits online training of OSTs, we defined the conductance state for simulation. The multiple conductance state G_I was measured at saturation time, which is defined as the time t when conductance exhibits deviations $\Delta G_I(t) = 1 - |I_t/I_{t-0.05}| < 0.5\%$, where $\Delta G_I(t)$ is the variation at time t, I_t is the current at t, and $I_{t-0.05}$ is the current of the previous measurement point, with 0.05 s as the time between successive measurements. The input image is passed through the various layers and classified (Figure 6a).[60] The potentiation and depression cycles were consistently repeated over 1,000 spikes (Figure 6b). 60 000 images were used for training and 10 000 images were used for testing to calculate the recognition accuracy with the 20 epochs.[55] The ideal numerical results showed 96.7% recognition accuracy for the 8×8 MNIST simulation and 98.0% recognition accuracy for the 28×28 MNIST simulation. Our IGOST showed recognition accuracy of 95.8% for the 8×8 MNIST simulation and 96.0% for the 28×28 MNIST simulation (Figure 6c,d). Considering the device-to-device deviation, recognition accuracy was calculated as 93.6% for the 8×8 MNIST simulation and 95.5% for the 28×28 MNIST simulation, which show lower accuracy than single device (Figure S7, Supporting Information) These results demonstrate that appropriate molecular engineering to control the microstructure in films has achieved the
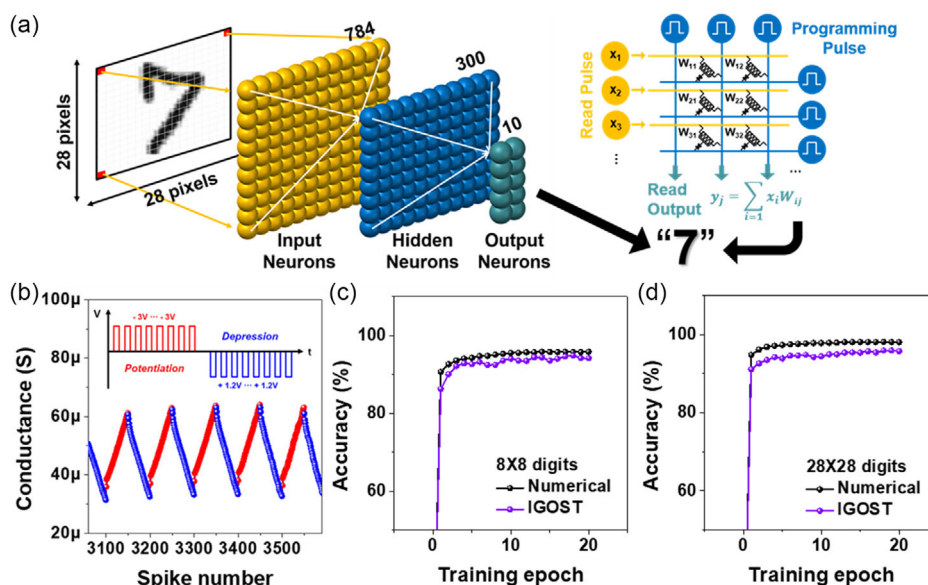

Figure 6. Simulation of pattern recognition with the optimized DPP-OST array (29SVS_Ann). a) A schematic of the pattern recognition for 28×28 pixel handwritten digits. b) 50 potentiation and depression cycles from writing (−3 V) and erasing operation (+1.2 V) with spike duration and time interval of 80 ms. For reading, drain voltage = −0.4 V was used. Recognition accuracy of c) small digits (8×8) and d) large digits (28×28) in MNIST simulation.

**ADVANCED
SCIENCE NEWS**

www.advancedsciencenews.com

**ADVANCED
INTELLIGENT
SYSTEMS**

www.advintellsyst.com

long-term plasticity of DPP-OSTs and their applicability as components in neuromorphic computing.

3. Conclusion

We suggest a facile approach that uses molecular engineering to increase synaptic retention time of the DPP-OSTs. To determine the effect of the molecular structure of DPP-SVS polymers on synaptic retention time of the OSTs, by changing alkyl spacer lengths of the DPP-SVS, the molecular structure of the DPP-SVS is modulated. Subsequent thermal annealing further improves the microstructure of the film to have better crystallinity. Increase in side chain length and thermal annealing caused increase in the chain ordering, orientation, and grain size of the DPP-SVS films. The 29SVS_Ann DPP-OST showed the highest PPF and EPSC gain in SRDP for STP and the longest retention time for LTP. The steric hindrance between ions and alkyl side chain is proposed to explain the effect of side-chain length in synaptic behavior. The time-depedent UV–vis absorption spectra during real-time electrochemical reaction can prove that side-chain engineering affected the doping concentrations and dedoping rates of the 24SVS_Ann and 29SVS_Ann; small steric hindrance of 29SVS_Ann induces electrochemically favorable ion doping. In addition, high crystallinity of 29SVS_Ann also suppresses back-diffusion of penetrated ions, so the 29SVS_Ann shows slow synaptic decay behavior. In simulations, an ANN composed of DPP-OSTs that used 29SVS_Ann achieved accuracy ≈96.0% in recognition of MNIST handwritten digits. Our molecular tailoring strategies to control the synaptic retention time of the intrinsic polymer semiconductors provides useful guildeline to engineer the molecular structure of semiconducting polymers for use in neuromorphic computing.

4. Experimental Section

Device Fabrication: Poly-[2,5-bis(2-decyltetradecyl)pyrrolo[3,4-c]pyrrole-1,4-(2H,5H)-dione-(E)-(1,2-bis(5-(thiophen-2-yl)selenophen-2-yl)ethene] (24SVS; $M_n = 101$ kDa, PDI = 1.70) and poly [2,5-bis(7-decylnonadecyl)pyrrolo [3,4-c]pyrrole-1,4(2H,5H)-dione-(E)-1,2-bis(5-(thiophen-2-yl)selenophen-2-yl)ethene] (29SVS; $M_n = 127$ kDa, PDI = 1.28) were synthesized using a palladium-catalyzed Stille coupling reaction as reported previously.[40] The surfaces of the glass substrates were modified using SAM treatment.[61] The glass substrates were first cleaned with acetone and isopropyl alcohol in an ultrasonic bath and then dried. Then 2.4 mM octadecyltrimethoxysilane (Sigma Aldrich) solution in trichloroethylene (>99%, Sigma-Aldrich) was spin coated on a UV/ozone-cleaned substrate at 2000 rpm for 30 s. The substrates were stored in vacuum for 12 h with an open vial that contained 10 mL of ammonium hydroxide solution (25% in water, Sigma-Aldrich). Then the substrates were rinsed in toluene and dried at room temperature. The iongel was obtained by mixing ionic liquid 1-Ethyl-3-methylimidazolium bis(trifluoromethylsulfonyl)imide ([EMIM][TFSI], Sigma-Aldrich) and poly(styrene-block-methyl methacyrlate-block-styrene) triblock copolymer (PS-PMMA-PS, Polymer Source) in ethyl acetate (Sigma-Aldrich) (1:9:90 in weight). The DPP-SVS solutions were prepared in chlorobenzene (Sigma-Aldrich) at the concentration of 5 mg mL^{-1} and then spin coated at 1000 rpm for 60 s on the SAM-treated glass substrates. The films were thermally annealed at 200 °C for 10 min in N$_2$ glovebox. The pristine films were held in a vacuum chamber to completely evaporate the solvent. As source and drain electrodes, 50 nm-thick gold was deposited on the films by thermal evaporation through shadow masks in a high-vacuum chamber (≈10^{-6} Torr). For

all the devices, the channel length was 50 μm and the channel width was 1500 μm. Subsequently, ion gel was drop cast on the channel regions and then dried in a vacuum chamber for 12 h.

Device Characterization: Synchrotron-based 2D GIXD was performed on all the films at the 3C, 6D, and 9 A beam lines at the Pohang Accelerator Laboratory (PAL, Republic of Korea). AFM (Multimode 8, Bruker) was performed on the same batch samples.[62] UV–vis absorption spectra of films were measured using a UV–vis spectrophotometer (Lambda 465, Perkin Elmer). For time-dependent UV–vis absorption spectral measurements, −3 V of voltage was applied to Pt wire for 30 s during the doping process. 45 s of dedoping process was conducted without any electrical bias to confirm reverse electrochemical reaction. DPP copolymer-coated ITO substrate was grounded to induce an electrochemical reaction of the polymer film. All electrical characteristics were measured using a Keysight B1500A semiconductor device analyzer under N$_2$ in a glovebox.

MNIST Simulation: The crossbar array simulation of ANNs was simulated using the "Cross Sim" platform (Sandia National Laboratory, USA). The MNIST dataset of 60 000 handwritten digits was used for training, using backpropagation. Then 10 000 handwritten digits were used for the recognition accuracy test. A three-layer network (input neurons, hidden neurons, and output neurons) was used for MNIST simulation. 8 bits were used for analog to digital converter (ADC)/digital to analog converter (DAC) in peripheral circuits for MNIST simulation.

Supporting Information

Supporting Information is available from the Wiley Online Library or from the author.

Conflict of Interest

The authors declare no conflict of interest.

Data Availability Statement

The data that support the findings of this study are available in the Supporting Information of this article.

[1] M. A. Ungless, X. Gasull, E. T. Walters, *J. Neurophysiol.* **2002**, *87*, 2408.
[2] J. L. McGaugh, *Science* **2000**, *287*, 248.

**ADVANCED
SCIENCE NEWS**

www.advancedsciencenews.com

**ADVANCED
INTELLIGENT
SYSTEMS**

www.advintellsyst.com

[3] L. F. Abbott, W. G. Regehr, *Nature* **2004**, *431*, 796.

[4] T. C. Südhof, *Neuron* **2013**, *80*, 675.

[5] J. F. Otto, Y. Yang, W. N. Frankel, H. S. White, K. S. Wilcox, *J. Neurosci.* **2006**, *26*, 2053.

[6] A. L. Hodgkin, A. F. Huxley, *J. Physiol.* **1952**, *117*, 500.

[7] V. M. Ho, J.-A. Lee, K. C. Martin, *Science* **2011**, *334*, 623.

[8] H.-L. Park, Y. Lee, N. Kim, D.-G. Seo, G.-T. Go, T.-W. Lee, *Adv. Mater.* **2019**, *0*, 1903558.

[9] Y. Kim, A. Chortos, W. Xu, Y. Liu, J. Y. Oh, D. Son, J. Kang, A. M. Foudeh, C. Zhu, Y. Lee, S. Niu, J. Liu, R. Pfattner, Z. Bao, T.-W. Lee, *Science* **2018**, *360*, 998.

[10] H.-L. Park, H. Kim, D. Lim, H. Zhou, Y.-H. Kim, Y. Lee, S. Park, T.-W. Lee, *Adv. Mater.* **2020**, *32*, 1906899.

[11] S.-H. Lee, H.-L. Park, C.-M. Keum, I.-H. Lee, M.-H. Kim, S.-D. Lee, *Phys. Status Solidi R* **2019**, *13*, 1900044.

[12] S. H. Lee, H. L. Park, M. H. Kim, S. Kang, S. D. Lee, *ACS Appl. Mater. Interfaces* **2019**, *11*, 30108.

[13] H. L. Park, M. H. Kim, S. H. Lee, *Adv. Electron. Mater.* **2020**, *6*, 2000582.

[14] H.-L. Park, T.-W. Lee, *Org. Electron.* **2021**, *98*, 106301.

[15] D.-G. Seo, G.-T. Go, H.-L. Park, T.-W. Lee, *MRS Bull.* **2021**, *46*, 321.

[16] W. Xu, T. L. Nguyen, Y.-T. Kim, C. Wolf, R. Pfattner, J. Lopez, B.-G. Chae, S.-I. Kim, M. Y. Lee, E.-Y. Shin, Y.-Y. Noh, J. H. Oh, H. Hwang, C.-G. Park, H. Y. Woo, T.-W. Lee, *Nano Energy* **2018**, *48*, 575.

[17] X. Chen, B. Chen, B. Jiang, T. Gao, G. Shang, S. Han, C. Kuo, V. A. L. Roy, Y. Zhou, *Adv. Funct. Mater.* **2023**, *33*, 2208807.

[18] X. Liu, F. Wang, J. Su, Y. Zhou, S. Ramakrishna, *Adv. Funct. Mater.* **2022**, *32*, 2113050.

[19] W. Xu, S.-Y. Min, H. Hwang, T.-W. Lee, *Sci. Adv.* **2016**, *2*, e1501326.

[20] Y. Lee, H.-L. Park, Y. Kim, T.-W. Lee, *Joule* **2021**, *5*, 794.

[21] Y. Lee, T.-W. Lee, *Acc. Chem. Res.* **2019**, *52*, 964.

[22] Y. Lee, J. Y. Oh, W. Xu, O. Kim, T. R. Kim, J. Kang, Y. Kim, D. Son, J. B. H. Tok, M. J. Park, Z. Bao, T.-W. Lee, *Sci. Adv.* **2018**, *4*, eaat7387.

[23] K.-N. Kim, M.-J. Sung, H.-L. Park, T.-W. Lee, *Adv. Electron. Mater.* **2021**, *8*, 2100935.

[24] S. Desbief, M. di Lauro, S. Casalini, D. Guerin, S. Tortorella, M. Barbalinardo, A. Kyndiah, M. Murgia, T. Cramer, F. Biscarini, D. Vuillaume, *Org. Electron.* **2016**, *38*, 21.

[25] G.-T. Go, Y. Lee, D.-G. Seo, M. Pei, W. Lee, H. Yang, T.-W. Lee, *Adv. Intell. Syst.* **2020**, *2*, 2000012.

[26] D. G. Seo, Y. Lee, G. T. Go, M. Pei, S. Jung, Y. H. Jeong, W. Lee, H. L. Park, S. W. Kim, H. Yang, C. Yang, T. W. Lee, *Nano Energy* **2019**, *65*, 104035.

[27] Y. van de Burgt, A. Melianas, S. T. Keene, G. Malliaras, A. Salleo, *Nat. Electron.* **2018**, *1*, 386.

[28] T. Marszalek, M. Li, W. Pisula, *Chem. Commun.* **2016**, *52*, 10938.

[29] K. Müllen, W. Pisula, *J. Am. Chem. Soc.* **2015**, *137*, 9503.

[30] Q. Liu, S. E. Bottle, P. Sonar, *Adv. Mater.* **2020**, *32*, 1900382.

[31] T. Lei, M. Guan, J. Liu, H. C. Lin, R. Pfattner, L. Shaw, A. F. McGuire, T. C. Huang, L. Shao, K. T. Cheng, J. B. H. Tok, Z. Bao, *Proc. Natl. Acad. Sci. U. S. A.* **2017**, *114*, 5107.

[32] J. Xu, S. Wang, G. N. Wang, C. Zhu, S. Luo, L. Jin, X. Gu, S. Chen, V. R. Feig, J. W. F. To, S. Rondeau-gagné, J. Park, B. C. Schroeder, C. Lu, J. Y. Oh, Y. Wang, Y. Kim, H. Yan, R. Sinclair, D. Zhou, G. Xue, B. Murmann, C. Linder, W. Cai, J. B. Tok, *Science* **2017**, *355*, 59.

[33] I. Kang, T. K. An, J. A. Hong, H. J. Yun, R. Kim, D. S. Chung, C. E. Park, Y. H. Kim, S. K. Kwon, *Adv. Mater.* **2013**, *25*, 524.

[34] J. Y. Back, H. Yu, I. Song, I. Kang, H. Ahn, T. J. Shin, S. K. Kwon, J. H. Oh, Y. H. Kim, *Chem. Mater.* **2015**, *27*, 1732.

[35] Y. Zhang, Q. Zeng, Y. Shen, L. Yang, F. Yu, *ACS Appl. Mater. Interfaces* **2020**, *12*, 56216.

[36] Y. Lee, Y. Liu, D.-G. Seo, J. Y. Oh, Y. Kim, J. Li, J. Kang, J. Kim, J. Mun, A. M. Foudeh, Z. Bao, T.-W. Lee, *Nat. Biomed. Eng.* **2022**, *7*, 511.

[37] E. M. Izhikevich, *IEEE Trans. Neural Networks* **2003**, *14*, 1569.

[38] H. Wang, Q. Zhao, Z. Ni, Q. Li, H. Liu, Y. Yang, L. Wang, Y. Ran, Y. Guo, W. Hu, Y. Liu, *Adv. Mater.* **2018**, *30*, 1803961.

[39] T. Ohno, T. Hasegawa, T. Tsuruoka, K. Terabe, J. K. Gimzewski, M. Aono, *Nat. Mater.* **2011**, *10*, 591.

[40] I. Kang, H. J. Yun, D. S. Chung, S. K. Kwon, Y. H. Kim, *J. Am. Chem. Soc.* **2013**, *135*, 14896.

[41] H. Yu, K. H. Park, I. Song, M. J. Kim, Y. H. Kim, J. H. Oh, *J. Mater. Chem. C* **2015**, *3*, 11697.

[42] Y. Lei, P. Deng, J. Li, M. Lin, F. Zhu, T. W. Ng, C. S. Lee, B. S. Ong, *Sci. Rep.* **2016**, *6*, 24476.

[43] U. Holzwarth, N. Gibson, *Nat. Nanotechnol.* **2011**, *6*, 534.

[44] H. W. Lin, W. Y. Lee, W. C. Chen, *J. Mater. Chem.* **2012**, *22*, 2120.

[45] J. O. Guardado, A. Salleo, *Adv. Funct. Mater.* **2017**, *27*, 1701791.

[46] E. M. Thomas, M. A. Brady, H. Nakayama, B. C. Popere, R. A. Segalman, M. L. Chabinyc, *Adv. Funct. Mater.* **2018**, *28*, 1803687.

[47] L. Q. Flagg, C. G. Bischak, J. W. Onorato, R. B. Rashid, C. K. Luscombe, D. S. Ginger, *J. Am. Chem. Soc.* **2019**, *141*, 4345.

[48] L. F. Abbott, S. B. Nelson, *Nat. Neurosci.* **2000**, *3*, 1178.

[49] G. Rachmuth, H. Z. Shouval, M. F. Bear, C.-S. Poon, *Proc. Natl. Acad. Sci* **2011**, *108*, E1266 LP.

[50] T. V. P. Bliss, S. F. Cooke, *Clinics* **2011**, *66*, 3.

[51] G. Bornschein, O. Arendt, S. Hallermann, S. Brachtendorf, J. Eilers, H. Schmidt, *J. Physiol.* **2013**, *591*, 3355.

[52] R. S. Zucker, W. G. Regehr, *Annu. Rev. Physiol.* **2002**, *64*, 355.

[53] Y. Li, Y. Zhong, J. Zhang, L. Xu, Q. Wang, H. Sun, H. Tong, X. Cheng, X. Miao, *Sci. Rep.* **2014**, *4*, 4906.

[54] M. J. Panzer, C. D. Frisbie, *J. Am. Chem. Soc.* **2007**, *129*, 6599.

[55] J. Rivnay, S. Inal, B. A. Collins, M. Sessolo, E. Stavrinidou, X. Strakosas, C. Tassone, D. M. Delongchamp, G. G. Malliaras, *Nat. Commun.* **2016**, *7*, 287.

[56] S. Inal, G. G. Malliaras, J. Rivnay, *J. Mater. Chem. C* **2016**, *4*, 3942.

[57] Z. Wang, Z. Liu, L. Ning, M. Xiao, Y. Yi, Z. Cai, A. Sadhanala, G. Zhang, W. Chen, H. Sirringhaus, D. Zhang, *Chem. Mater.* **2018**, *30*, 3090.

[58] Y. Van De Burgt, E. Lubberman, E. J. Fuller, S. T. Keene, G. C. Faria, S. Agarwal, M. J. Marinella, A. Alec Talin, A. Salleo, *Nat. Mater.* **2017**, *16*, 414.

[59] E. J. Fuller, F. El Gabaly, F. Léonard, S. Agarwal, S. J. Plimpton, R. B. Jacobs-Gedrim, C. D. James, M. J. Marinella, A. A. Talin, *Adv. Mater.* **2017**, *29*, 1604310.

[60] L. Yann, C. Corinna, C. J. C. Burges, The MNIST Database of Handwritten Digits, National Institute of Standards and Technology, Gaithersburg, MD **2016**, http://yann.lecun.com/exdb/mnist/.

[61] Y. Ito, A. A. Virkar, S. Mannsfeld, J. H. Oh, M. Toney, J. Locklin, Z. Bao, *J. Am. Chem. Soc.* **2009**, *131*, 9396.

[62] C. Y. Gao, M. Pei, H. J. Choi, H. Yang, *Adv. Funct. Mater.* **2019**, *29*, 1903163.